Research article

A musculoskeletal finite element model of rat knee joint for evaluating cartilage biomechanics during gait

*Gustavo A. Orozco[1,2], Kalle Karjalainen[1], Eng Kuan Moo[1,3], Lauri Stenroth[1,4], Petri Tanska[1], Jaqueline Lourdes Rios[3,5], Teemu V. Tuomainen[1], Mikko J. Nissi[1], Hanna Isaksson[2], Walter Herzog[3], Rami K. Korhonen[1]

[1]*Department of Applied Physics, University of Eastern Finland, Kuopio, Finland Yliopistonranta 1, FI-70210 Kuopio, Finland*

[2]*Department of Biomedical Engineering, Lund University, Box 188, 221 00, Lund, Sweden*

[3]*Faculty of Kinesiology, Human Performance Laboratory, University of Calgary, 2500, University Drive NW, Calgary, Alberta, Canada T2N1N4*

[4]*Department of Biomedical Sciences, University of Copenhagen, Denmark*

[5]*Regenerative Medicine Center Utrecht, University Medical Center Utrecht, Utrecht, Netherlands*

Keywords: rat knee joint, articular cartilage, finite element model, degeneration, gait cycle, MRI

Short title: Rat knee joint computational model

Corresponding author:

*Gustavo A. Orozco
Department of Applied Physics, University of Eastern Finland, Kuopio, Finland
Yliopistonranta 1, 70210 Kuopio, FI
Tel: +358 50 3485018
gustavo.orozco@uef.fi

Abstract

Abnormal loading of the knee due to injuries or obesity is thought to contribute to the development of osteoarthritis (OA). Small animal models have been used for studying OA progression mechanisms. However, numerical models to study cartilage responses under dynamic loading in preclinical animal models have not been developed. Here we present a musculoskeletal finite element (FE) model of a rat knee joint to evaluate cartilage biomechanical responses during a gait cycle. The rat knee joint geometries were obtained from a 3-D MRI dataset and the boundary conditions regarding loading in the joint were extracted from a musculoskeletal model of the rat hindlimb. The fibril-reinforced poroelastic (FRPE) properties of the rat cartilage were derived from data of mechanical indentation tests. Our numerical results showed the relevance of simulating anatomical and locomotion characteristics in the rat knee joint for estimating tissue responses such as contact pressures, stresses, strains, and fluid pressures. We found that the contact pressure and maximum principal strain were virtually constant in the medial compartment whereas they showed the highest values at the beginning of the gait cycle in the lateral compartment. Furthermore, we found that the maximum principal stress increased during the stance phase of gait, with the greatest values at midstance. We anticipate that our approach serves as a first step towards investigating the effects of gait abnormalities on the adaptation and degeneration of rat knee joint tissues and could be used to evaluate biomechanically-driven mechanisms of the progression of OA as a consequence of joint injury or obesity.

Author Summary

Osteoarthritis is a disease of the musculoskeletal system which is characterized by the degradation of articular cartilage. Changes in the knee loading after injuries or obesity contribute to the development of cartilage degeneration. Since injured cartilage cannot be reversed back to intact conditions, small animal models have been widely used for investigating osteoarthritis progression mechanisms. Moreover, experimental studies have been complemented with numerical models to overcome inherent limitations such as cost, difficulties to obtain accurate measures and replicate degenerative situations in the knee joint. However, computational models to study articular cartilage responses under dynamic loading in small animal models have not been developed. Thus, here we present a musculoskeletal finite element model of a rat knee joint to evaluate cartilage biomechanical responses during gait. Our computational model considers both the anatomical and locomotion characteristics of the rat knee joint for estimating mechanical responses in the articular cartilage. We suggest that our approach can be used to investigate tissue adaptations based on the mechanobiological responses of the cartilage to prevent the progression of osteoarthritis.

Introduction

Abnormal loading of the knee joint after overuse, severe injuries, or obesity are risk factors of cartilage degeneration, contributing to the development of osteoarthritis (OA) [1]. OA is the most common musculoskeletal disorder and among the most frequent causes of pain, physical disability, and economic loss worldwide [2]. Currently, there is no cure for OA, and patients with end-stage OA must undergo a total joint replacement to recover mobility and relieve the pain. Although it is understood that the mechanical environment plays a role in the onset and development of OA, the mechanisms leading to the progression of OA remain largely unknown, thereby preventing the development of effective measures to stop or slow down the degeneration of the joint [3,4].

In order to comprehend the degenerative mechanisms, preclinical animal models have been used in orthopaedic research for studying the initiation and progression of OA [5–7]. In preclinical research, small animal models (e.g., rodents) are commonly used as they are cost-effective and take less time to respond to an intervention compared to large animal models [8]. Invasive and non-invasive models have been developed to study different OA phenotypes. For example, invasive models utilize surgical injuries (ACL transection, meniscectomy, and destabilization of medial meniscus (DMM)) or chemical interventions to induce cartilage degradation (intra-articular injections of proinflammatory cytokines) [9,10]. On the other hand, noninvasive models include load-induced impact injury, cyclic joint loading, or spontaneous/genetic OA development [11–13].

Experimental studies have been complemented with numerical models to overcome inherent limitations such as cost, challenges to obtain accurate measures experimentally *in vivo*, and replicate degenerative scenarios in the knee joint. Finite element (FE) models have been used to investigate knee joint function during locomotion and joint loading alterations, as well as the associated adaptation and degeneration in the joint tissues [14,15]. For instance, subject-specific FE models of the knee joint have been developed to study the biomechanical responses of articular cartilage and meniscus after ACL rupture and reconstruction [16,17]. These computational models include realistic knee tissue geometries acquired from magnetic resonance imaging (MRI) data, complex material models to account for tissue anisotropy,

and dynamic loading from a patient´s gait or other relevant motion, to provide insights into the role of biomechanics in the development of OA. Since physiological changes in articular cartilage occur faster in rodents, these realistic numerical models would be helpful to investigate the effect of treatments on cartilage tissue. Nevertheless, only a few simplified FE models for joints of rodents have been reported in the literature [18,19]. In previous studies, micro-computed tomography (μCT) imaging was used to obtain the geometry of the cartilages, bone, and meniscus that were subsequently implemented in FE models [20,21]. However, those studies assumed the cartilage thickness based on the proximal tibia and distal femur segmentations, simulated simplified loading conditions in the numerical model (e.g., only standing posture), and adopted cartilage tissue to be isotropic and linearly elastic, limiting the use of these models in preclinical rodent studies of OA.

In order to use FE modeling to understand mechanisms leading to OA in animal models, a methodology has to be developed first. In this study, we developed an FE model of a rat knee joint to estimate articular cartilage biomechanics during the stance phase of gait. The FE model included a fibril-reinforced poroelastic (FRPE) material model that accounts for material nonlinearities of meniscus and cartilages, as well as their nonfibrillar and fibrillar matrices. The FRPE properties of the rat cartilage were obtained by fitting the model to previous indentation experiments [22]. Knee joint loading was computed using a validated musculoskeletal model of the rat hindlimb [23] and was used to define the boundary conditions of the FE model. The knee joint functions, as well as forces, stresses, strains, and fluid pressures, were assessed within the femoral and tibial cartilages, and menisci. We suggest that this animal-specific approach could be useful for understanding mechanisms leading to OA progression and may offer valuable insights when evaluating potential treatments in preclinical animal models.

Materials and Methods

Magnetic resonance imaging protocol and segmentation. An intact right lower limb of a cadaveric rat without known musculoskeletal disorders (Sprague Dawley, 56-week-old male, body weight = 5.5 N) was immersed in a phosphate buffered saline solution and imaged at room temperature using an 11.74T μMRI

scanner in combination with a 10-mm diameter proton RF coil (UltraShield 500 MHz, Bruker BioSpin MRI GmbH, Ettlingen, Germany). MRI was conducted at the facilities of the Kuopio Biomedical Imaging Unit at A.I. Virtanen Institute of Molecular Sciences (University of Eastern Finland, Kuopio, Finland). The MRI data was acquired using ParaVision 6.0.1. software (Bruker) and a 3-D multi-echo gradient echo (MGE) pulse sequence. The imaging parameters were: echo time (TE) = 1.8, 4.9, 8.0, 11.1, 14.2, and 17.3 ms, repetition time (TR) = 100 ms, flip angle (FA) = 20°, field of view (FOV) =14.25 × 9.5 × 9.5 mm^3, echo spacing (ES) = 3.1 ms, averages = 1, scan time = 1h 49 min, receiver bandwidth = 0.15 MHz and an acquisition matrix of 384 × 256 × 256, yielding an isotropic voxel size of 37µm.

Knee joint geometries that included femoral and tibial cartilages, menisci, collateral, and cruciate ligament insertions were segmented using the open software 3DSlicer (http://www.slicer.org)[24] from the MRI data acquired with the shortest TE. The segmented geometries were imported into Abaqus (v2018; Dassault Systèmes Simulia Corp, Providence, RI) where the FE meshes were constructed using 8-node hexahedral linear poroelastic (C3D8P) elements (Fig 1).

Fig. 1 here.

Fig 1. Workflow of the study. (a) Rat knee geometry, (b) motion and loading during gait from a musculoskeletal model, and (c) FRPE material properties from indentation tests were implemented into (d) the FE model. e) Knee tissues' mechanical responses were evaluated during the stance phase of the gait cycle.

Musculoskeletal modeling of rat hindlimb. We utilized a previously validated musculoskeletal model of the right hindlimb of Sprague-Dawley rat in OpenSim (SimTK, Stanford, CA) [23,25] (https://simtk.org/projects/rat_hlimb_model). The model was used to determine the knee joint contact forces and lower extremity muscle forces occurring during the gait cycle, which were used as boundary conditions for the FE knee joint model [26]. Briefly, the musculoskeletal model was composed of four body segments, including accurate representations of the bones (spine, femur, tibia, and foot), 14 degrees of freedom, and

171 39 muscle-tendon actuators that are represented as linear elements in each muscle segment. We prescribed
172 the joint angle profiles during the stance phase of gait by scaling the locomotion and ground reaction force
173 (GRF) data from Charles et al. [27,28] to match the normal (healthy) gait pattern of Sprague-Dawley rats
174 reported in previous experimental studies [29–34]. The scaling of the joint angle-time curves was conducted
175 using a custom MATLAB script (R2019b; The MathWorks, Natick, MA). Scaled joint angles and GRFs
176 were used for estimating the muscle forces using static optimization (e.g. minimizing the cost function
177 associated with muscle activations) and subsequently performed the joint reaction analysis. Finally, the
178 musculoskeletal model outputs: the flexion-extension angle, valgus-varus and internal-external passive
179 moments, and translational knee forces (distal-proximal, medial-lateral, and anterior-posterior) were used
180 to drive the knee joint FE model, by following a similar protocol as previously published [16,35,36] (Fig
181 2).
182
183 **Fig. 2 here.**
184 **Fig 2.** Gait data for the computational model of the rat knee joint. External-internal and valgus-varus
185 moments, and flexion-extension rotation. In addition, anterior-posterior, distal-proximal, and medial-lateral
186 translational forces were implemented in the FE model of the knee joint. The inputs of the FE joint model
187 (joint kinematics and translational forces) were similar to previous experimental studies with Sprague-
188 Dawley rats [29–34].
189
190 **Biomechanical articular cartilage characterization.** The fibril-reinforced poroelastic (FRPE) properties
191 of healthy Sprague-Dawley rat cartilage were characterized using previously published experimental
192 indentation measurements [22]. The FRPE cartilage parameters were obtained by fitting the stress relaxation
193 curve of the FE model to the mean stress relaxation curve collected from healthy control animals (n = 6) of
194 a previous study [22]. Briefly, stress relaxation experiments were performed using a spherical indenter (r =
195 175 ± 2.5 μm, 316 L glass) that was mounted to a multiaxial load cell (force resolution: Fz =3.5 mN and Fx
196 = Fy = 2.5 mN) and a three-axis mechanical tester (Mach-1 v500css, Biomomentum, QC, Canada). For each

specimen, the tibial cartilage was fixed in a specimen holder using dental cement and immersed in a phosphate buffered saline solution. To ensure proper sample-indenter contact for consistent and repeatable measurements, an automatic contact criterion of 0.01 N (contact velocity: 0.1 mm/s) was applied to all the samples. Then a single stress-relaxation step (indentation amplitude: 0.04 mm (~30% of uncompressed cartilage thickness), compression velocity: 0.04 mm/s, relaxation time: 400 s) was performed on 11 sites each for the lateral and medial tibial cartilage using the automated indentation mapping system (Fig 1c). After the indentation experiments, the thickness was measured on new 11 sites (located close to those previously identified for the indentation mapping) each for the lateral and medial tibial cartilage using automated thickness mapping with a needle probe.

Subsequently, six axisymmetric FE models of a cylindrical specimen (radius: 1.5 mm) that took into account sample-specific thickness were constructed in Abaqus to simulate the mean of the indentation tests for each sample. The sample height was set to be the mean cartilage thickness measured for each sample (see Table S1 in the **supplementary material**). The geometry was meshed by 825 linear axisymmetric pore pressure continuum elements (element type CAX4P). Mesh convergence was ensured for each model. An FRPE constitutive formulation was implemented for simulating the articular cartilage response [37,38]. Specifically, the material model assumes that cartilage tissue is composed of solid and fluid matrices. The solid matrix is separated into a porous non-fibrillar part, representing the proteoglycan matrix, and an elastic fibrillar network, describing the collagen fibrils. The total stress is given by

$$\boldsymbol{\sigma}_{\mathrm{tot}} = \boldsymbol{\sigma}_{\mathrm{s}} + \boldsymbol{\sigma}_{\mathrm{fl}} = \boldsymbol{\sigma}_{\mathrm{f}} + \boldsymbol{\sigma}_{\mathrm{nf}} - p\mathbf{I}, \tag{1}$$

where $\boldsymbol{\sigma}_{\mathrm{tot}}$ is the total stress tensor, $\boldsymbol{\sigma}_{\mathrm{s}}$ and $\boldsymbol{\sigma}_{\mathrm{fl}}$ represent the stress tensors of the solid matrix and interstitial fluid, respectively, p is the hydrostatic pressure, $\mathbf{I}$ is the unit tensor, and $\boldsymbol{\sigma}_{\mathrm{f}}$ and $\boldsymbol{\sigma}_{\mathrm{nf}}$ are the stress tensors of the fibrillar and non-fibrillar matrices, respectively. A neo-Hookean material is utilized to define the non-fibrillar component, in which the stress tensor is given by

$$\boldsymbol{\sigma}_{\mathrm{nf}} = \frac{1}{2} K_{\mathrm{nf}} \left(J - \frac{1}{J}\right)\mathbf{I} + \frac{G_{\mathrm{nf}}}{J}\left(\mathbf{F}\cdot\mathbf{F}^{\mathrm{T}} - J^{\frac{2}{3}}\mathbf{I}\right), \tag{2}$$

where K_{nf} and G_{nf} are the bulk and the shear moduli of the non-fibrillar matrix and J is the determinant of the deformation gradient tensor $\mathbf{F}$. The bulk (K_{nf}) and shear (G_{nf}) moduli of the non-fibrillar matrix are established as

$$K_{\mathrm{nf}} = \frac{E_{\mathrm{nf}}}{3(1-2\nu_{\mathrm{nf}})}\,, \tag{3}$$

$$G_{\mathrm{nf}} = \frac{E_{\mathrm{nf}}}{2(1+\nu_{\mathrm{nf}})}\,, \tag{4}$$

where E_{nf} and ν_{nf} are the Young´s modulus and the Poisson´s ratio of the non-fibrillar matrix. Then, the stresses in the elastic collagen fibrils are given by

$$\sigma_{\mathrm{f}} = \begin{cases} E_{\mathrm{f}}\,\varepsilon_{\mathrm{f}}\,, & \varepsilon_{\mathrm{f}} > 0 \\ 0, & \varepsilon_{\mathrm{f}} \le 0 \end{cases}, \tag{5}$$

where σ_{f} and ε_{f} represent the stress and strain of the fibril, and E_{f} is the fibril network modulus [38]. Therefore, collagen fibrils support tension only. The fibril network stress emerges from the sum of the primary and secondary collagen fibril stresses, which are computed individually for each integration point in each element [39]. The stresses for these fibrils in tension are defined

$$\begin{cases} \sigma_{\mathrm{f},i}^{\mathrm{p}} = \rho_z C \sigma_{\mathrm{f}} \\ \sigma_{\mathrm{f},i}^{\mathrm{s}} = \rho_z \sigma_{\mathrm{f}} \end{cases}, \tag{6}$$

where $\sigma_{\mathrm{f},i}^{\mathrm{p}}$ and $\sigma_{\mathrm{f},i}^{\mathrm{s}}$ are the stresses for primary and secondary fibrils, respectively, ρ_z is the relative collagen density, and C is the density ratio between primary and secondary fibrils. Then, the total stress tensor of the fibrillar network is defined as the sum of the stresses in each fibril ($\sigma_{\mathrm{f},i}$):

$$\boldsymbol{\sigma}_{\mathrm{f}} = \sum_{i}^{totf} \sigma_{\mathrm{f},i}\,\vec{e}_{\mathrm{f},i} \otimes \vec{e}_{\mathrm{f},i} = \sum_{i}^{totf,\mathrm{p}} \sigma_{\mathrm{f},i}^{\mathrm{p}}\,\vec{e}_{\mathrm{f},i}^{\mathrm{p}} \otimes \vec{e}_{\mathrm{f},i}^{\mathrm{p}} + \sum_{i}^{totf,\mathrm{s}} \sigma_{\mathrm{f},i}^{\mathrm{s}}\,\vec{e}_{\mathrm{f},i}^{\mathrm{s}} \otimes \vec{e}_{\mathrm{f},i}^{\mathrm{s}}\,, \tag{7}$$

where *totf* is the total number of fibrils, $\vec{e}_{\mathrm{f},i}$ is the fibril orientation vector, $totf,\mathrm{p}$ and $totf,\mathrm{s}$ are the total number of primary and secondary fibrils, respectively, and $\vec{e}_{\mathrm{f},i}^{\mathrm{p}}$ and $\vec{e}_{\mathrm{f},i}^{\mathrm{s}}$ are the primary and secondary fibril orientation unit vectors, and $\otimes$ represent the outer product. Moreover, the fluid flow in the non-fibrillar matrix is assumed to follow Darcy´s law:

$$q = -k\nabla p\,, \tag{8}$$

where q is the fluid flux in the non-fibrillar matrix, ∇p is the hydrostatic pressure gradient vector across the region, and k is the hydraulic permeability. The hydraulic permeability is defined to be strain-dependent:

$$k = k_0\left(\frac{e+1}{1+e_0}\right)^M = k_0 J^M, \tag{9}$$

where k_0 is the initial permeability, M is a positive constant, and e and e_0 are the current and initial void ratios, respectively [39]. The void ratio e is expressed by the ratio of the fluid to the solid volumetric fraction:

$$e = \frac{n_{\mathrm{fl}}}{n_{\mathrm{s}}}\,, \tag{10}$$

where n_{s} is the solid volume fraction and n_{fl} is the fluid volume fraction.

The following boundary conditions were used for the axisymmetric FE models, similar to previous reports [37,40]. The bottom of the cartilage sample was fixed in the axial and lateral directions and fluid flow was allowed through the free non-contacting surfaces. However, no fluid flow was allowed to occur at the bottom surface. The contact between the indenter (simulated as a rigid analytical surface) and cartilage surface was assumed impermeable and frictionless. The cartilage sample was subjected to the indentation protocol described earlier in this study. In addition, the FRPE material properties (E_{f},E_{nf},k_0, and M) were obtained by minimizing the normalized mean squared error between the experimentally measured and the FE model-predicted forces using a minimum search algorithm (*fminsearch* function) in combination with Abaqus [37]. Poisson´s ratio of the nonfibrillar matrix was assumed to be 0.42 [40,41], leading to an effective (i.e. apparent) cartilage Poisson's ratio of ~0.1.

Finite element model of the rat knee joint. Cartilages and menisci were modeled using the FRPE material. For tibial and femoral cartilages, the fitted FRPE material parameters, depth-dependent collagen fibril architecture, and fluid fraction distribution were implemented [36,42,43]. The tibial cartilage-bone interface was fixed in all directions and bones were assumed rigid. For the menisci, the primary fibrils of the collagen network were oriented circumferentially, and the fluid fraction was assumed to be homogeneously

266 distributed [44–46]. Menisci properties were adopted based on earlier experiments on human meniscus due
267 to a lack of information about rat menisci properties in the literature. In addition, the roots of the menisci
268 were attached to the bone using linear spring elements with a total stiffness of 350 N/mm at each root [47].
269 A complete list of the material parameters used is given in Table 1.
270
271 **Table 1 -** Material parameters implemented for cartilage and menisci.

Material parameter	Cartilage	Menisci
E_f (MPa)	3.13†	3.79□
E_{nf} (MPa)	0.83†	0.08*
k_0 (10^{-15}m^{4}N^{-1}s^{-1})	3.30†	0.08*
ν	0.42§	0.3*
M	1.67†	12.1*
C	12.16**	12.16**
n_{fl}	$0.8 - 0.15h$**	0.72‡

272
273 E_f = fibril network modulus, E_{nf} = nonfibrillar matrix modulus, k_0= initial permeability, ν = Poisson´s ratio
274 of the nonfibrillar matrix, M = exponential term for the strain-dependent permeability, C = ratio of primary
275 to secondary collagen fibers, n_{fl} = depth-wise fluid fraction distribution, E_Θ = circumferential Young´s
276 modulus of menisci, $n_{f,p}$= number of primary fibrils and h indicates the normalized distance from the
277 cartilage surface (surface = 0, bottom = 1).
278
279 †Obtained from fitting the model to indentation experiments.
280 □The fibril network modulus of menisci was computed as follows: $E_f = \frac{E_\Theta}{C \times n_{f,p}} = \frac{184}{12.16 \times 4} = 3.79$ MPa
281 *Danso et al. [44,45]
282 **Wilson et al. [39]
283 ‡Makris et al. [48]
284 ‡‡Mow and Ratcliffe. [49]
285 §Korhonen et al., Mäkelä et al. [40,50]

Cruciate ligaments (ACL and PCL) and collateral ligaments (MCL and LCL) were modeled using spring elements with a bilinear behavior. The ligaments were assumed to be pre-elongated (MCL and LCL = 4% [51], ACL and PCL = 5% [36]) of the initial length at the segmented distance by using the bilinear spring selection. The stiffness of the ligaments (MCL 20 N/mm, LCL 20 N/mm, ACL 35 N/mm, and PCL 35 N/mm) were obtained from previous rat ligaments experimental studies [52,53]. The springs were attached to the center of the anatomical attachment sites of each ligament measured from MRI data [36,42]. Ligament anchorage points were fixed at the tibial bone sites during the gait cycle. The anchorage points at the femoral site were coupled to the main reference point (located at the midpoint between the condyles of the femur), allowing them to move along with the rigid bone.

The following boundary conditions were applied to the FE model of the rat knee joint. The stance phase of the rat's gait obtained from the musculoskeletal model was implemented to drive the FE simulation, similarly to that described in human knee joint studies [36,42]. In detail, after an initial contact step, the flexion-extension angle, and joint moments and translational forces during the stance phase were computed and implemented to the main reference point, located at the mid-point between the lateral and medial epicondyles of the femur (Fig 1). Surface-to-node contacts with frictionless sliding properties were applied between the cartilage-cartilage and cartilage-meniscus contact surfaces. The average and maximum tissue mechanical responses, including maximum principal stress, maximum principal strain, and fluid pressure were analyzed in the knee joint during the entire stance phase of the gait cycle. For evaluating the average tissue responses, average values over the cartilage-cartilage contact area were computed as a function of time.

Results

FRPE characterization of articular cartilage. The FRPE material model successfully described the response obtained from the indentation experiments, revealing R^2 = 0.97 ± 0.03 for the coefficient of determination. The optimized FRPE parameters E_f, E_{nf}, k_0, and M (mean ± standard deviation) were 3.13 ±

311 2.56 MPa, 0.83 ± 0.21 MPa, 3.30 ± 3.00 × 10^{-15} $m^4N^{-1}s^{-1}$, and 1.67 ± 0.62, respectively. Subsequently, the
312 mean value of each optimized cartilage parameter was used for the FE knee joint model (Table 1).
313
314 **Finite element model of the rat knee joint.** The FE rat knee joint model showed that the maximum
315 principal stress was concentrated on a small area at the beginning of the stance phase (Fig 3). Total
316 tibiofemoral reaction forces obtained in the medial and lateral compartments are presented in Figs. 4a and
317 4b, respectively. The model calculated the highest tibiofemoral reaction forces (1.16 BW) at ~55% of the
318 stance phase. Furthermore, the secondary knee kinematics displayed an increase in the posterior-anterior
319 and medial-lateral translations at the end of the stance phase (Figs 4c-d). In contrast, the inferior-superior
320 translation decreased with time during stance (Fig 4e). Additionally, the valgus-varus and external-internal
321 rotations increased with stance time (Figs 4f-g).
322
323 **Figs. 3 and 4 here.**
324 **Fig 3.** Maximum principal stress distribution in the femoral and tibial cartilages, and menisci calculated
325 from the FE model of the knee joint during the stance phase of the gait cycle (Lat: lateral: Med: medial).
326 The cartilage stresses obtained from the FE model agree with previous numerical studies on mice knee joints
327 under axial compressive forces [18,21].
328
329 **Fig 4.** Total tibiofemoral joint reaction force in the (a) medial and (b) lateral compartments, respectively.
330 Translations (c-e) and rotations (f, g) of the tibia with respect to the femur during the stance phase of gait
331 were also presented.
332
333 Quantitative analysis of the average tissue mechanical responses over the cartilage-cartilage contact
334 area within the medial and lateral compartments of the tibial cartilage during the stance phase of gait is
335 presented in Fig 5. The average contact pressure and maximum principal strain were virtually constant in
336 the medial compartment (0.02 MPa and 10.0%, respectively) whereas, in the lateral compartment, the

337 average contact pressure and maximum principal strain showed the highest values (0.06 MPa and 30%,
338 respectively) at the start of the stance phase and subsequently contact pressure and principal strain decreased
339 with time (Figs 5a-d). Moreover, the average maximum principal stress and fluid pressure within the medial
340 compartment were highest at midstance (5.6 and 4.8 MPa, respectively). In contrast, the average maximum
341 principal stress and fluid pressure in the lateral compartment decreased with time. Similar to the contact
342 pressure and maximum principal strain response, the highest stress and fluid pressure in the lateral
343 compartment occurred at the beginning of the stance phase. Peak contact pressures, stresses, strains, and
344 fluid pressures within the medial and lateral compartment as a function of stance are presented in Fig S1
345 (See the **supplementary material**).

346 The cruciate ligaments (ACL and PCL) in the knee joint experienced higher loads than the collateral
347 ligaments (MCL and LCL) throughout the stance phase (Fig 6). The force in the ACL was higher than that
348 in the PCL. The ACL force decreased from 0 to 30% of the stance phase and then increased until the end of
349 the stance phase (peak ACL load: 3.8 N). In contrast, the PCL force increased from 0 to ~40% of the stance
350 but then decreased until the end of the stance phase (peak PCL load: 2.1 N). Similar to the ACL response,
351 the MCL force (peak MCL load: ~1 N) decreased steadily from the beginning of the stance phase and
352 became virtually unloaded at midstance but increased slightly in the second half of the stance phase.
353 Conversely, the LCL force decreased at the start of the stance phase but revealed a minor increase from
354 ~20% of stance until the end of the gait cycle (peak LCL load: ~0.6 N).
355
356 **Figs. 5 and 6 here.**
357 **Fig 5.** Average contact pressure, maximum principal strain, maximum principal stress, and fluid pressure in
358 the contact area of the medial (a, c, e, and g) and lateral (b, d, f, and h) tibial cartilage surfaces during the
359 stance phase of gait. The contact stresses were similar to a previous study published by Gardner-Morde et
360 al. [20] where average contact stresses in the medial and lateral compartment at the reference loading state
361 were 0.4 and 0.1 MPa, respectively.
362

363 **Fig 6.** Forces transmitted through the cruciate ligaments (ACL and PCL) and collateral ligaments (MCL
364 and LCL) of the knee joint during the stance phase of gait.
365
366 ## Discussion
367 **Summary.** In the present study, we described a workflow for the generation and simulation of a finite
368 element model of a rat knee joint to estimate the biomechanical responses of articular cartilage and other
369 knee joint tissues during the stance phase of walking. To the best of our knowledge, this approach represents
370 the first 3-D rat knee model that can be used to investigate the cartilage and meniscus stresses and strains
371 from dynamic joint loading during gait. The rat knee joint geometries were extracted from a 3-D MRI dataset
372 and the boundary conditions regarding loading of the joint were extracted from a musculoskeletal model of
373 the rat hindlimb. In addition, the FRPE properties of the rat cartilage were derived from data of mechanical
374 indentation testing across the articular surfaces of the rat knee. Our numerical results showed the effect of
375 simulating anatomical and locomotion characteristics on the rat knee joint for estimating tissue responses,
376 such as contact pressures, stresses, strains, and fluid pressures, which can be used to estimate
377 mechanobiological changes of tissues during OA as well as to evaluate the effect of knee joint disorders and
378 gait impairments on articular cartilage in preclinical models of joint injury and disease [54].
379
380 **Biomechanical evaluation of articular cartilage.** Fibril-reinforced poroelastic (FRPE) properties of
381 cartilage in the rat knee joint were obtained using indentation experiments in the tibial plateau, combined
382 with FE models and an optimization algorithm. Although previous studies have measured cartilage
383 poroelastic properties during creep experiments in rat tibial cartilage [55], femoral cartilage [56,57], and
384 mouse tibial plateau [58], our study constitutes the first investigation to describe effectively the mechanical
385 behavior of cartilage of rat knee by using the mechanical moduli of the collagen fibril network and the non-
386 fibrillar solid matrix. In a previous study, Athanasiou et al. [56] performed indentation experiments on rat
387 articular cartilage. The aggregate compressive modulus (comparable to the nonfibrillar matrix modulus E_{nf})
388 and permeability of normal/healthy cartilage were 0.75 ± 0.16 MPa and 3.13 ± 2.59 × 10^{-15} $m^4N^{-1}s^{-1}$,

389 respectively. These findings are in agreement with the results of the present study, in which only healthy rat
390 cartilage tissue was used.

391 Our FE rat knee joint model was able to describe the stress, strain, and contact pressure distributions
392 on cartilage and menisci during the stance phase of gait. Numerical results revealed that the average cartilage
393 contact pressure remained almost constant in the medial compartment, but in the lateral compartment the
394 average contact pressure varied during the gait cycle. In a previous study, Gardner-Morde et al. [20]
395 estimated compressive contact stresses using discrete element analysis of the rat tibiofemoral joint during
396 standing with different applied varus loads without menisci. Average contact stresses in the medial and
397 lateral compartment at the reference loading state were 0.4 and 0.1 MPa, respectively. These contact stresses
398 were of similar magnitude to those reported in this study, in which the meniscus was included in the
399 simulation (0.1 MPa peak contact pressure).

400 On the other hand, the stress distributions indicated that the medial compartment experienced an
401 increase in the maximum principal stress during gait, while the lateral tibial compartment revealed
402 decreasing values during the second half of the stance phase. The stress distributions and forces indicated
403 that the meniscus provides substantial mechanical support during dynamic gait loading. The magnitude of
404 the cartilage stresses obtained from the FE model agrees with computational studies on mice knee joints
405 under axial compressive forces [18,21].

406 Regarding the notable mechanical support provided by the meniscus during gait loading, cartilage-
407 meniscus force represented 36% and 42% of the total reaction force within the medial and lateral
408 compartments in the midstance phase of walking (See Fig S2 in the **supplementary material**). This finding
409 is in good agreement with previous observations in mouse FE knee models under weight-bearing conditions,
410 where the cartilage-cartilage contact was reduced by 34% in the presence of the meniscus on the lateral
411 condyle [19,21]. Potentially, our numerical model could elucidate the mechanisms behind the progressive
412 structural changes observed in DMM surgical instability pre-clinical models of OA [59]. Also, for
413 investigating the effect of refining surgical small rodent models of OA on both joint pathology and pain
414 response [60].

ACL and PCL forces were the largest knee joint ligament forces throughout the entire stance phase of gait. This finding supports previous observations that these ligaments are the main joint stabilizers, controlling the anterior-posterior translation of the tibia [61,62]. It is known that ACL and PCL deficiency has an influence on knee joint kinematics and kinetics, increasing the stress concentration in certain areas of the articular cartilage and leading to cartilage degeneration [63–65]. In fact, preclinical posttraumatic OA animal models following ACL rupture have been widely developed [66–68]. Potentially, our current numerical approach can be used to investigate the progression of OA following ACL transection by considering the effect of gait impairments and weight-bearing alterations on the function of the rat knee joint and subsequent changes in the cartilage tissue [5,69,70].

Limitations. Our study contains limitations regarding the FE model development, animal gait motion, tissue mechanical characterization, and specific assumptions. First, knee tissue geometries were based on a single male Sprague Dawley rat. This single joint might not represent all anatomical details of the rat knee across animals and rat strains, but it is practical for this proof-of-concept study. In the future, a large number of animals should be studied to consider different anatomical characteristics of articular cartilage as a function of age, sex, diet, etc. Second, the gait motion used to drive the FE knee model was extracted from a previous validated musculoskeletal model in combination with a generic locomotion pattern of Sprague-Dawley rats reported in the literature [29–34]. This approach might not completely represent all the hindlimb motion details of an animal during a full gait cycle. However, using generic locomotion data from the literature was sufficient for the methodological development required in this study. In the future, we plan to obtain animal-specific motion using 3-D X-Ray Reconstruction of Moving Morphology (XROMM) [71] in combination with musculoskeletal modeling to acquire the ground reaction forces, moments, and accurate and subject-specific hindlimb kinematics of rats. Third, we did not consider the patella and tendons in the FE model. This might represent differences in the rotations and joint reaction force, but we would not expect greater variations of cartilage stresses and strains than observed in this simpler model. Our workflow could be applied to generate complex models with additional anatomical features, such as the kneecap, tendons, and

441 muscles. We acknowledge that these additional aspects could be included but the animal-specific motion
442 and a more sophisticated musculoskeletal model are necessary to validate the above-mentioned details.
443 Fourth, the characterization of the biomechanical properties of rat cartilage considered only a single stress-
444 relaxation step during a single indentation experiment in tibial cartilage. It was assumed that the femoral
445 cartilage had the same properties as the tibial cartilage. More stress-relaxation steps should be performed to
446 characterize the intrinsic nonlinearities of cartilage tissue across all joint surfaces, and additional mechanical
447 testing (e.g. shear, tension, unconfined compression, and confined compression) should be done to
448 complement the currently available cartilage responses. Fifth, in order to overcome the lack of information
449 on the material properties of the menisci in the rat knee joint, we used values from previous experimental
450 studies [44,72]. Characterization of rat meniscus material properties and implementation of these properties
451 into FE models are part of our upcoming plan. Although experimental tests on rat ligaments and tendons
452 are challenging to conduct due to the small size of the samples, it is worth characterizing both the nonlinear
453 toe and linear regions of the ligaments for a better understanding of the function of ligaments and tendons
454 in healthy, injured, and diseased knees [73]. Sixth, volumetric information of the healthy tibiofemoral joint
455 of the rat was obtained using the presented MRI acquisition scheme with a high isotropic resolution of 37
456 μm (using an 11.74T μMRI scanner). As the femoral and tibial cartilage thickness is approximately 180
457 μm, the resolution allowed for four to five pixels across the cartilage thickness, which may affect the
458 accuracy of tissue detection. Partial volume artifacts could further affect the segmentation, but the high
459 resolution utilized helps mitigate this effect. Previous research [74,75] was performed using anisotropic
460 pixels with pixel sizes greater ($59 \times 117 \times 234$ μm^3 and $51 \times 51 \times 94$ μm^3, respectively) than those
461 used in our work. In addition, chemical shift of the fat, emphasized by the ultra-high field of the magnet
462 (11.74T), may cause errors in the estimation of tissue volumes. The studies mentioned above utilized fat
463 suppression methods in their gradient echo acquisition schemes [74,75]. Here, fat suppression was not used
464 in the main acquisition to preserve as much signal as possible, as preliminary images with fat suppression
465 suggested minimal effect.
466

Future developments.

Our model of the rat knee provides a potential numerical tool to estimate the loading and changes in articular cartilage and other tissues of the rat knee during the stance phase of gait after pre-clinical OA interventions in rodents. Cartilage tissue mechanical responses, such as stress, strain, and fluid velocity have been reported as indicators of tissue adaptation and degradation after joint injury and/or disease [16,76,77]. For example, our knee model allows for simulating the effects of ACL transection and partial/total meniscectomy on the compositional and structural changes in cartilage based on mechanobiological response. In this context, the FE models can be used to investigate the effects of interventions in animal models and to estimate adaptations in mechanical properties of knee joint tissues. Furthermore, our numerical model could be used to study the effects of exercise and prebiotic supplementation, described in OA animal models of diet-induced obesity [11,12,78]. For instance, we could combine the body weight, locomotion, and structural properties with cartilage degenerative algorithms in our FE model for predicting OA progression [76,79].

Longitudinal observations of OA progression have been conducted using quantitative μMRI in the knee joints of rats subjected to different interventions [80,81]. These cartilage properties obtained from MRI could be included in the FE model for evaluating the structural progression of OA as well as for validating the numerical predictions driven by different degenerative mechanisms.

Conclusions. We present a workflow for the generation and simulation of FE models of the rat knee joint. Our model considers both the anatomical and locomotion characteristics of the rat knee joint for estimating tissue mechanical responses in the articular cartilage. In the future, we will expand this approach to investigate tissue adaptations based on the mechanobiological response of the cartilage tissue to controlled interventions. Thus, our numerical FE model employing FRPE material properties may allow for studying the mechanisms leading to changes in composition and structure in cartilage after a traumatic injury or specific pre-clinical interventions. After these evaluations and further validation of the numerical predictions, this model could be applied in the planning of joint loading to prevent the progression of knee joint OA.

Acknowledgments

The authors appreciate the support of the University of Eastern Finland, Lund University, and the University of Calgary to undertake this study.

Author contributions

Conceptualization: GAO, KK, EKM, LS, PT, JLR, TVT, MJN, HI, WH, RKK

Data curation: GAO, KK, LS, PT, TVT, MJN

Formal analysis: GAO, KK, LS, TVT, MJN

Funding acquisition: PT, MJN, HI, WH, RKK

Investigation: GAO, KK, EKM, LS, PT, JLR, TVT, MJN, HI, WH, RKK

Methodology: GAO, KK, EKM, LS, PT, JLR, TVT, MJN, HI, WH, RKK

Project administration: HI, WH, RKK

Resources: HI, WH, RKK

Software: GAO, KK

Supervision: EKM, LS, PT, MJN, HI, WH, RKK

Validation: GAO

Visualization: GAO

Writing– original draft: GAO

Writing–review & editing: GAO, KK, EKM, LS, PT, JLR, TVT, MJN, HI, WH, RKK

Data availability

The datasets generated and analyzed during this study are available from the corresponding author on a reasonable request.

Compliance with Ethical Standards

Funding

We acknowledge funding support from the European Union's Horizon 2020 research and innovation programme under the Marie Skłodowska-Curie grant agreement No 713645, Strategic Funding of the University of Eastern Finland, Academy of Finland (grant nos. 285909, 324529, 324994, 328920, 332915, 334773 - under the frame of ERA PerMed), Swedish Research Council (2019-00953 - under the frame of ERA PerMed), European Regional Development Fund, Innovation Fund Denmark (9088-00006B - under the frame of ERA PerMed), Finnish Cultural Foundation (grant #191044 and #200059), Maire Lisko Foundation, Sigrid Juselius Foundation, Päivikki ja Sakari Sohlberg Foundation, Maud Kuistila Memorial Foundation, Saastamoinen Foundation, The Killam Foundation, The Canada Research Chair Programme and The Canadian Institutes for Health Research.

Conflict of interest

The authors declare no potential conflict of interest.

References

1. Zhang Y, Jordan JM. Epidemiology of Osteoarthritis. Clin Geriatr Med. 2010;26: 355–369. doi:10.1016/j.cger.2010.03.001

2. Brown TD, Johnston RC, Saltzman CL, Marsh JL, Buckwalter JA. Posttraumatic osteoarthritis: a first estimate of incidence, prevalence, and burden of disease. J Orthop Trauma. 2006;20: 739–744. doi:10.1097/01.bot.0000246468.80635.ef

3. Anderson DD, Chubinskaya S, Guilak F, Martin JA, Oegema TR, Olson SA, et al. Post-traumatic osteoarthritis: improved understanding and opportunities for early intervention. J Orthop Res. 2011;29: 802–809. doi:10.1002/jor.21359

4. Kramer WC, Hendricks KJ, Wang J. Pathogenetic mechanisms of posttraumatic osteoarthritis: opportunities for early intervention. Int J Clin Exp Med. 2011;4: 285–298.

5. Clarke KA, Heitmeyer SA, Smith AG, Taiwo YO. Gait analysis in a rat model of osteoarthrosis. Physiol Behav. 1997;62: 951–954. doi:10.1016/s0031-9384(97)00022-x

6. Griffin TM, Huebner JL, Kraus VB, Yan Z, Guilak F. Induction of osteoarthritis and metabolic inflammation by a very high-fat diet in mice: effects of short-term exercise. Arthritis Rheum. 2012;64: 443–453. doi:10.1002/art.33332

7. Lakes EH, Allen KD. Gait analysis methods for rodent models of arthritic disorders: reviews and recommendations. Osteoarthr Cartil. 2016;24: 1837–1849. doi:10.1016/j.joca.2016.03.008

8. Adebayo OO, Holyoak DT, van der Meulen MCH. Mechanobiological Mechanisms of Load-Induced Osteoarthritis in the Mouse Knee. J Biomech Eng. 2019;141. doi:10.1115/1.4043970

9. Jacobs BY, Kloefkorn HE, Allen KD. Gait analysis methods for rodent models of osteoarthritis. Curr Pain Headache Rep. 2014;18: 456. doi:10.1007/s11916-014-0456-x

10. Iijima H, Aoyama T, Tajino J, Ito A, Nagai M, Yamaguchi S, et al. Subchondral plate porosity colocalizes with the point of mechanical load during ambulation in a rat knee model of post-traumatic osteoarthritis. Osteoarthritis Cartilage. 2016;24: 354–363. doi:10.1016/j.joca.2015.09.001

568 11. Griffin TM, Fermor B, Huebner JL, Kraus VB, Rodriguiz RM, Wetsel WC, et al. Diet-induced obesity
569 differentially regulates behavioral, biomechanical, and molecular risk factors for osteoarthritis in
570 mice. Arthritis Res Ther. 2010;12: R130. doi:10.1186/ar3068

571 12. Rios JL, Bomhof MR, Reimer RA, Hart DA, Collins KH, Herzog W. Protective effect of prebiotic
572 and exercise intervention on knee health in a rat model of diet-induced obesity. Sci Rep. 2019;9: 3893.
573 doi:10.1038/s41598-019-40601-x

574 13. Brown SB, Hornyak JA, Jungels RR, Shah YY, Yarmola EG, Allen KD, et al. Characterization of
575 Post-Traumatic Osteoarthritis in Rats Following Anterior Cruciate Ligament Rupture by Non-Invasive
576 Knee Injury (NIKI). J Orthop Res. 2020;38: 356–367. doi:10.1002/jor.24470

577 14. Gu KB, Li LP. A human knee joint model considering fluid pressure and fiber orientation in cartilages
578 and menisci. Med Eng Phys. 2011;33: 497–503. doi:10.1016/j.medengphy.2010.12.001

579 15. Bolcos PO, Mononen ME, Tanaka MS, Yang M, Suomalainen J-S, Nissi MJ, et al. Identification of
580 locations susceptible to osteoarthritis in patients with anterior cruciate ligament reconstruction:
581 Combining knee joint computational modelling with follow-up T1ρ and T2 imaging. Clin Biomech
582 (Bristol, Avon). 2019; 104844. doi:10.1016/j.clinbiomech.2019.08.004

583 16. Orozco GA, Bolcos P, Mohammadi A, Tanaka MS, Yang M, Link TM, et al. Prediction of local fixed
584 charge density loss in cartilage following ACL injury and reconstruction: A computational proof-of-
585 concept study with MRI follow-up. J Orthop Res. 2020. doi:10.1002/jor.24797

586 17. Halonen KS, Mononen ME, Töyräs J, Kröger H, Joukainen A, Korhonen RK. Optimal graft stiffness
587 and pre-strain restore normal joint motion and cartilage responses in ACL reconstructed knee. Journal
588 of Biomechanics. 2016;49: 2566–2576. doi:10.1016/j.jbiomech.2016.05.002

589 18. Borges PDN, Forte AE, Vincent TL, Dini D, Marenzana M. Rapid, automated imaging of mouse
590 articular cartilage by microCT for early detection of osteoarthritis and finite element modelling of
591 joint mechanics. Osteoarthritis and Cartilage. 2014;22: 1419–1428. doi:10.1016/j.joca.2014.07.014

592 19. Gu XI, Leong D, Maldonado N, Williams EA, Sun HB, Cardoso L. Finite Element Modeling of Rat
593 Knee Joint for the Study of Tibio-Femoral Contact. ORS 2011 Annual Meeting Procedures. 2011; 1.

20. Gardner-Morse M, Badger G, Beynnon B, Roemhildt M. Changes in in vitro compressive contact stress in the rat tibiofemoral joint with varus loading. J Biomech. 2013;46: 1216–1220. doi:10.1016/j.jbiomech.2013.01.009

21. Zanjani-Pour S, Giorgi M, Dall'Ara E. Development of Subject Specific Finite Element Models of the Mouse Knee Joint for Preclinical Applications. Front Bioeng Biotechnol. 2020;8. doi:10.3389/fbioe.2020.558815

22. Rios JL, Boldt KR, Mather JW, Seerattan RA, Hart DA, Herzog W. Quantifying the Effects of Different Treadmill Training Speeds and Durations on the Health of Rat Knee Joints. Sports Med Open. 2018;4: 15. doi:10.1186/s40798-018-0127-2

23. Johnson WL, Jindrich DL, Roy RR, Reggie Edgerton V. A three-dimensional model of the rat hindlimb: musculoskeletal geometry and muscle moment arms. J Biomech. 2008;41: 610–619. doi:10.1016/j.jbiomech.2007.10.004

24. Fedorov A, Beichel R, Kalpathy-Cramer J, Finet J, Fillion-Robin J-C, Pujol S, et al. 3D Slicer as an Image Computing Platform for the Quantitative Imaging Network. Magn Reson Imaging. 2012;30: 1323–1341. doi:10.1016/j.mri.2012.05.001

25. Johnson WL, Jindrich DL, Zhong H, Roy RR, Edgerton VR. Application of a rat hindlimb model: a prediction of force spaces reachable through stimulation of nerve fascicles. IEEE Trans Biomed Eng. 2011;58: 3328–3338. doi:10.1109/TBME.2011.2106784

26. Bolcos PO, Mononen ME, Mohammadi A, Ebrahimi M, Tanaka MS, Samaan MA, et al. Comparison between kinetic and kinetic-kinematic driven knee joint finite element models. Scientific Reports. 2018;8: 17351. doi:10.1038/s41598-018-35628-5

27. Charles JP, Cappellari O, Hutchinson JR. A Dynamic Simulation of Musculoskeletal Function in the Mouse Hindlimb During Trotting Locomotion. Front Bioeng Biotechnol. 2018;6. doi:10.3389/fbioe.2018.00061

28. Charles JP, Cappellari O, Spence AJ, Wells DJ, Hutchinson JR. Muscle moment arms and sensitivity analysis of a mouse hindlimb musculoskeletal model. J Anat. 2016;229: 514–535. doi:10.1111/joa.12461

29. Steiner R, Dhar M, Stephenson SM, Newby S, Bow A, Pedersen A, et al. Biometric Data Comparison Between Lewis and Sprague Dawley Rats. Front Vet Sci. 2019;6: 469. doi:10.3389/fvets.2019.00469

30. Dienes JA, Hu X, Janson KD, Slater C, Dooley EA, Christ GJ, et al. Analysis and Modeling of Rat Gait Biomechanical Deficits in Response to Volumetric Muscle Loss Injury. Front Bioeng Biotechnol. 2019;7: 146. doi:10.3389/fbioe.2019.00146

31. Webb AA, Kerr B, Neville T, Ngan S, Assem H. Kinematics and ground reaction force determination: a demonstration quantifying locomotor abilities of young adult, middle-aged, and geriatric rats. J Vis Exp. 2011. doi:10.3791/2138

32. Kelley BJ, Harel NY, Kim C-Y, Papademetris X, Coman D, Wang X, et al. Diffusion Tensor Imaging as a Predictor of Locomotor Function after Experimental Spinal Cord Injury and Recovery. J Neurotrauma. 2014;31: 1362–1373. doi:10.1089/neu.2013.3238

33. Eftaxiopoulou T, Macdonald W, Britzman D, Bull AMJ. Gait compensations in rats after a temporary nerve palsy quantified using temporo-spatial and kinematic parameters. J Neurosci Methods. 2014;232: 16–23. doi:10.1016/j.jneumeth.2014.04.011

34. Piet J, Mielke F, Veryser D, Lories R, Aerts P, Van Wassenbergh S, et al. Estimation of knee contact forces in the rat, based on integrated xromm setup data. Osteoarthritis and Cartilage. 2021;29: S174–S175. doi:10.1016/j.joca.2021.02.242

35. Venäläinen MS, Mononen ME, Salo J, Räsänen LP, Jurvelin JS, Töyräs J, et al. Quantitative Evaluation of the Mechanical Risks Caused by Focal Cartilage Defects in the Knee. Scientific Reports. 2016;6: 37538. doi:10.1038/srep37538

36. Halonen KS, Mononen ME, Jurvelin JS, Töyräs J, Korhonen RK. Importance of depth-wise distribution of collagen and proteoglycans in articular cartilage—A 3D finite element study of stresses and strains in human knee joint. Journal of Biomechanics. 2013;46: 1184–1192. doi:10.1016/j.jbiomech.2012.12.025

37. Ebrahimi M, Ojanen S, Mohammadi A, Finnilä MA, Joukainen A, Kröger H, et al. Elastic, Viscoelastic and Fibril-Reinforced Poroelastic Material Properties of Healthy and Osteoarthritic Human Tibial Cartilage. Ann Biomed Eng. 2019;47: 953–966. doi:10.1007/s10439-019-02213-4

38. Li LP, Soulhat J, Buschmann MD, Shirazi-Adl A. Nonlinear analysis of cartilage in unconfined ramp compression using a fibril reinforced poroelastic model. Clin Biomech (Bristol, Avon). 1999;14: 673–682. doi:10.1016/s0268-0033(99)00013-3

39. Wilson W, van Donkelaar CC, van Rietbergen B, Ito K, Huiskes R. Stresses in the local collagen network of articular cartilage: a poroviscoelastic fibril-reinforced finite element study. J Biomech. 2004;37: 357–366.

40. Mäkelä JTA, Han S-K, Herzog W, Korhonen RK. Very early osteoarthritis changes sensitively fluid flow properties of articular cartilage. J Biomech. 2015;48: 3369–3376. doi:10.1016/j.jbiomech.2015.06.010

41. Korhonen RK, Laasanen MS, Töyräs J, Lappalainen R, Helminen HJ, Jurvelin JS. Fibril reinforced poroelastic model predicts specifically mechanical behavior of normal, proteoglycan depleted and collagen degraded articular cartilage. J Biomech. 2003;36: 1373–1379.

42. Orozco GA, Tanska P, Mononen ME, Halonen KS, Korhonen RK. The effect of constitutive representations and structural constituents of ligaments on knee joint mechanics. Scientific Reports. 2018;8: 2323. doi:10.1038/s41598-018-20739-w

43. Mononen ME, Mikkola MT, Julkunen P, Ojala R, Nieminen MT, Jurvelin JS, et al. Effect of superficial collagen patterns and fibrillation of femoral articular cartilage on knee joint mechanics—A 3D finite element analysis. Journal of Biomechanics. 2012;45: 579–587. doi:10.1016/j.jbiomech.2011.11.003

44. Danso EK, Honkanen JTJ, Saarakkala S, Korhonen RK. Comparison of nonlinear mechanical properties of bovine articular cartilage and meniscus. J Biomech. 2014;47: 200–206. doi:10.1016/j.jbiomech.2013.09.015

45. Danso EK, Mäkelä JTA, Tanska P, Mononen ME, Honkanen JTJ, Jurvelin JS, et al. Characterization of site-specific biomechanical properties of human meniscus-Importance of collagen and fluid on mechanical nonlinearities. J Biomech. 2015;48: 1499–1507. doi:10.1016/j.jbiomech.2015.01.048

46. Fithian DC, Kelly MA, Mow VC. Material properties and structure-function relationships in the menisci. Clin Orthop Relat Res. 1990; 19–31.

675 47. Villegas DF, Maes JA, Magee SD, Haut Donahue TL. Failure properties and strain distribution
676 analysis of meniscal attachments. Journal of Biomechanics. 2007;40: 2655–2662.
677 doi:10.1016/j.jbiomech.2007.01.015

678 48. Makris EA, Hadidi P, Athanasiou KA. The knee meniscus: Structure–function, pathophysiology,
679 current repair techniques, and prospects for regeneration. Biomaterials. 2011;32: 7411–7431.
680 doi:10.1016/j.biomaterials.2011.06.037

681 49. Mow VC, Ratcliffe A. Structure and Function of Articular Cartilage and Meniscus. Philadelphia, PA:
682 Lippincott-Raven. 1997.

683 50. Korhonen RK, Laasanen MS, Töyräs J, Lappalainen R, Helminen HJ, Jurvelin JS. Fibril reinforced
684 poroelastic model predicts specifically mechanical behavior of normal, proteoglycan depleted and
685 collagen degraded articular cartilage. Journal of Biomechanics. 2003;36: 1373–1379.
686 doi:10.1016/S0021-9290(03)00069-1

687 51. Gantoi FM, Brown MA, Shabana AA. Finite Element Modeling of the Contact Geometry and
688 Deformation in Biomechanics Applications1. J Comput Nonlinear Dynam. 2013;8: 041013–041013.
689 doi:10.1115/1.4024541

690 52. Warden SJ, Saxon LK, Castillo AB, Turner CH. Knee ligament mechanical properties are not
691 influenced by estrogen or its receptors. Am J Physiol Endocrinol Metab. 2006;290: E1034-1040.
692 doi:10.1152/ajpendo.00367.2005

693 53. Zuckerman J, Stull GA. Effects of exercise on knee ligament separation force in rats. Journal of
694 Applied Physiology. 1969 [cited 25 Jun 2021]. doi:10.1152/jappl.1969.26.6.716

695 54. Jacobs BY, Dunnigan K, Pires-Fernandes M, Allen KD. Unique spatiotemporal and dynamic gait
696 compensations in the rat monoiodoacetate injection and medial meniscus transection models of knee
697 osteoarthritis. Osteoarthritis Cartilage. 2017;25: 750–758. doi:10.1016/j.joca.2016.12.012

698 55. Roemhildt ML, Beynnon BD, Gauthier AE, Gardner-Morse M, Ertem F, Badger GJ. Chronic in vivo
699 load alteration induces degenerative changes in the rat tibiofemoral joint. Osteoarthritis Cartilage.
700 2013;21: 346–357. doi:10.1016/j.joca.2012.10.014

701 56. Athanasiou KA, Zhu CF, Wang X, Agrawal CM. Effects of aging and dietary restriction on the
702 structural integrity of rat articular cartilage. Ann Biomed Eng. 2000;28: 143–149. doi:10.1114/1.238

703 57. Wang L, Kalu DN, Banu J, Thomas JB, Gabriel N, Athanasiou K. Effects of ageing on the
704 biomechanical properties of rat articular cartilage. Proc Inst Mech Eng H. 2006;220: 573–578.
705 doi:10.1243/09544119H04404

706 58. Cao L, Youn I, Guilak F, Setton LA. Compressive properties of mouse articular cartilage determined
707 in a novel micro-indentation test method and biphasic finite element model. J Biomech Eng. 2006;128:
708 766–771. doi:10.1115/1.2246237

709 59. Glasson SS, Blanchet TJ, Morris EA. The surgical destabilization of the medial meniscus (DMM)
710 model of osteoarthritis in the 129/SvEv mouse. Osteoarthritis Cartilage. 2007;15: 1061–1069.
711 doi:10.1016/j.joca.2007.03.006

712 60. Gowler PRW, Mapp PI, Burston JJ, Shahtaheri M, Walsh DA, Chapman V. Refining surgical models
713 of osteoarthritis in mice and rats alters pain phenotype but not joint pathology. PLOS ONE. 2020;15:
714 e0239663. doi:10.1371/journal.pone.0239663

715 61. Vaienti E, Scita G, Ceccarelli F, Pogliacomi F. Understanding the human knee and its relationship to
716 total knee replacement. Acta Biomed. 2017;88: 6–16. doi:10.23750/abm.v88i2-S.6507

717 62. Shelburne KB, Torry MR, Pandy MG. Muscle, ligament, and joint-contact forces at the knee during
718 walking. Med Sci Sports Exerc. 2005;37: 1948–1956. doi:10.1249/01.mss.0000180404.86078.ff

719 63. Abubakar MS, Nakamura S, Kuriyama S, Ito H, Ishikawa M, Furu M, et al. Influence of Posterior
720 Cruciate Ligament Tension on Knee Kinematics and Kinetics. The Journal of Knee Surgery. 2016;29:
721 684–689. doi:10.1055/s-0036-1571803

722 64. Kang K-T, Koh Y-G, Jung M, Nam J-H, Son J, Lee YH, et al. The effects of posterior cruciate ligament
723 deficiency on posterolateral corner structures under gait- and squat-loading conditions. Bone and Joint
724 Research. 2017;6: 31–42. doi:10.1302/2046-3758.61.BJR-2016-0184.R1

725 65. Lansdown DA, Pedoia V, Zaid M, Amano K, Souza RB, Li X, et al. Variations in Knee Kinematics
726 After ACL Injury and After Reconstruction Are Correlated With Bone Shape Differences. Clin Orthop
727 Relat Res. 2017;475: 2427–2435. doi:10.1007/s11999-017-5368-8

728 66. Wang L-J, Zeng N, Yan Z-P, Li J-T, Ni G-X. Post-traumatic osteoarthritis following ACL injury.
729 Arthritis Res Ther. 2020;22. doi:10.1186/s13075-020-02156-5

67. Ramme AJ, Lendhey M, Raya JG, Kirsch T, Kennedy OD. A novel rat model for subchondral microdamage in acute knee injury: a potential mechanism in post-traumatic osteoarthritis. Osteoarthritis and Cartilage. 2016;24: 1776–1785. doi:10.1016/j.joca.2016.05.017

68. Jay GD, Elsaid KA, Kelly KA, Anderson SC, Zhang L, Teeple E, et al. Prevention of cartilage degeneration and gait asymmetry by lubricin tribosupplementation in the rat following anterior cruciate ligament transection. Arthritis Rheum. 2012;64: 1162–1171. doi:10.1002/art.33461

69. Proffen BL, Sieker JT, Murray MM, Akelman MR, Chin KE, Perrone GS, et al. Extracellular Matrix-Blood Composite Injection Reduces Post-Traumatic Osteoarthritis After Anterior Cruciate Ligament Injury In the Rat. J Orthop Res. 2016;34: 995–1003. doi:10.1002/jor.23117

70. Allen KD, Mata BA, Gabr MA, Huebner JL, Adams SB, Kraus VB, et al. Kinematic and dynamic gait compensations resulting from knee instability in a rat model of osteoarthritis. Arthritis Res Ther. 2012;14: R78. doi:10.1186/ar3801

71. Brainerd EL, Baier DB, Gatesy SM, Hedrick TL, Metzger KA, Gilbert SL, et al. X-ray reconstruction of moving morphology (XROMM): precision, accuracy and applications in comparative biomechanics research. Journal of Experimental Zoology Part A: Ecological Genetics and Physiology. 2010;313A: 262–279. doi:https://doi.org/10.1002/jez.589

72. Dabiri Y, Li LP. Altered knee joint mechanics in simple compression associated with early cartilage degeneration. Comput Math Methods Med. 2013;2013: 862903. doi:10.1155/2013/862903

73. Ristaniemi A, Regmi D, Mondal D, Torniainen J, Tanska P, Stenroth L, et al. Structure, composition and fibril-reinforced poroviscoelastic properties of bovine knee ligaments and patellar tendon. J R Soc Interface. 2021;18: 20200737. doi:10.1098/rsif.2020.0737

74. Wang Y-XJ, Wang J, Deng M, Liu G, Qin L. In vivo three-dimensional magnetic resonance imaging of rat knee osteoarthritis model induced using meniscal transection. J Orthop Translat. 2015;3: 134–141. doi:10.1016/j.jot.2015.06.002

75. Goebel JC, Bolbos R, Pham M, Galois L, Rengle A, Loeuille D, et al. In vivo high-resolution MRI (7T) of femoro-tibial cartilage changes in the rat anterior cruciate ligament transection model of osteoarthritis: a cross-sectional study. Rheumatology (Oxford). 2010;49: 1654–1664. doi:10.1093/rheumatology/keq154

76. Eskelinen ASA, Mononen ME, Venäläinen MS, Korhonen RK, Tanska P. Maximum shear strain-based algorithm can predict proteoglycan loss in damaged articular cartilage. Biomech Model Mechanobiol. 2019;18: 753–778. doi:10.1007/s10237-018-01113-1

77. Hosseini SM, Veldink MB, Ito K, van Donkelaar CC. Is collagen fiber damage the cause of early softening in articular cartilage? Osteoarthr Cartil. 2013;21: 136–143. doi:10.1016/j.joca.2012.09.002

78. Sansone V, Applefield RC, De Luca P, Pecoraro V, Gianola S, Pascale W, et al. Does a high-fat diet affect the development and progression of osteoarthritis in mice?: A systematic review. Bone Joint Res. 2019;8: 582–592. doi:10.1302/2046-3758.812.BJR-2019-0038.R1

79. Liukkonen MK, Mononen ME, Vartiainen P, Kaukinen P, Bragge T, Suomalainen J-S, et al. Evaluation of the Effect of Bariatric Surgery-Induced Weight Loss on Knee Gait and Cartilage Degeneration. J Biomech Eng. 2018;140. doi:10.1115/1.4038330

80. Tsai P-H, Lee H-S, Siow TY, Chang Y-C, Chou M-C, Lin M-H, et al. Sequential Change in T2* Values of Cartilage, Meniscus, and Subchondral Bone Marrow in a Rat Model of Knee Osteoarthritis. PLOS ONE. 2013;8: e76658. doi:10.1371/journal.pone.0076658

81. Ali TS, Prasadam I, Xiao Y, Momot KI. Progression of Post-Traumatic Osteoarthritis in rat meniscectomy models: Comprehensive monitoring using MRI. Sci Rep. 2018;8: 6861. doi:10.1038/s41598-018-25186-1

783 **Figures**

784 **Fig 1.**

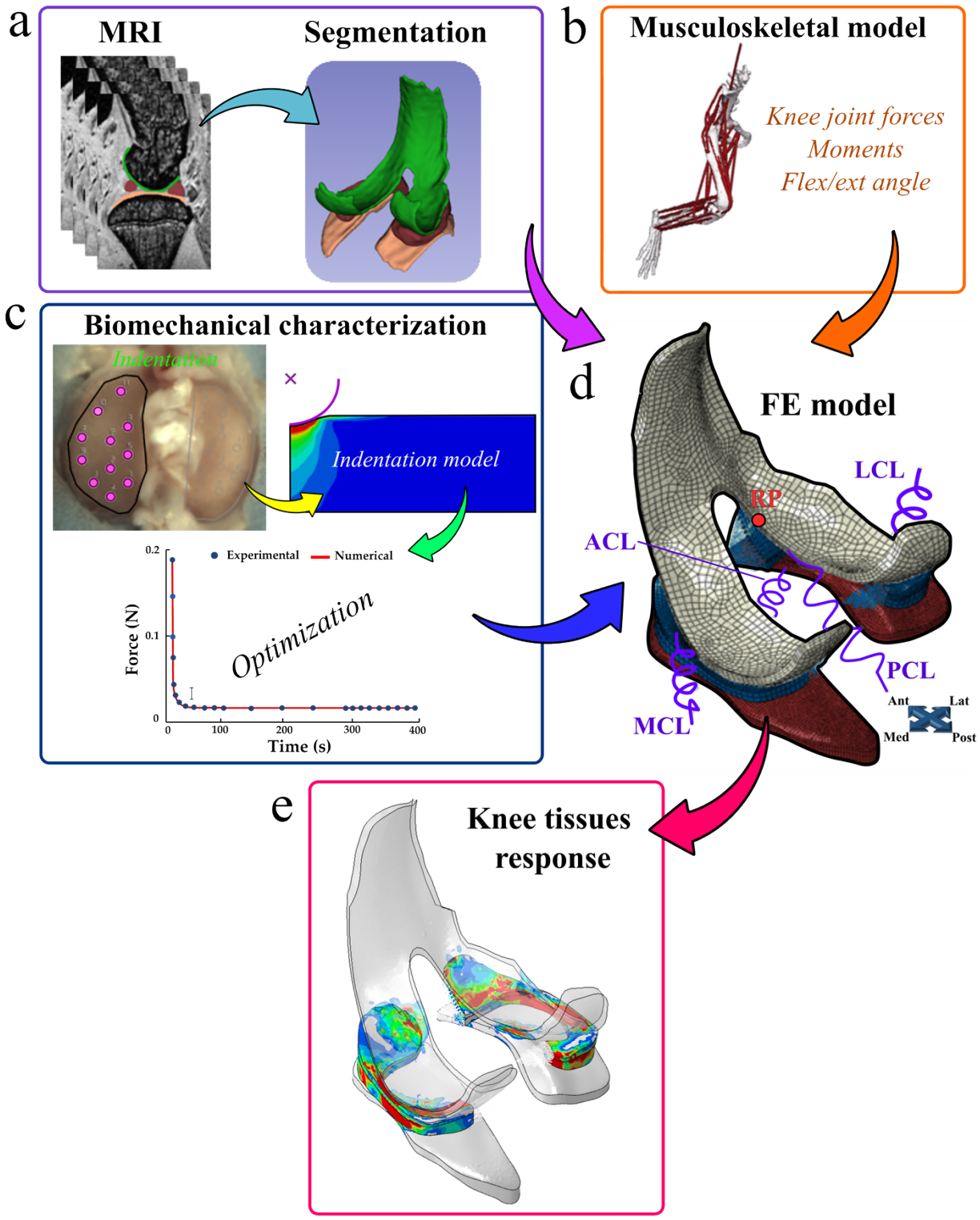

785

Fig 2.

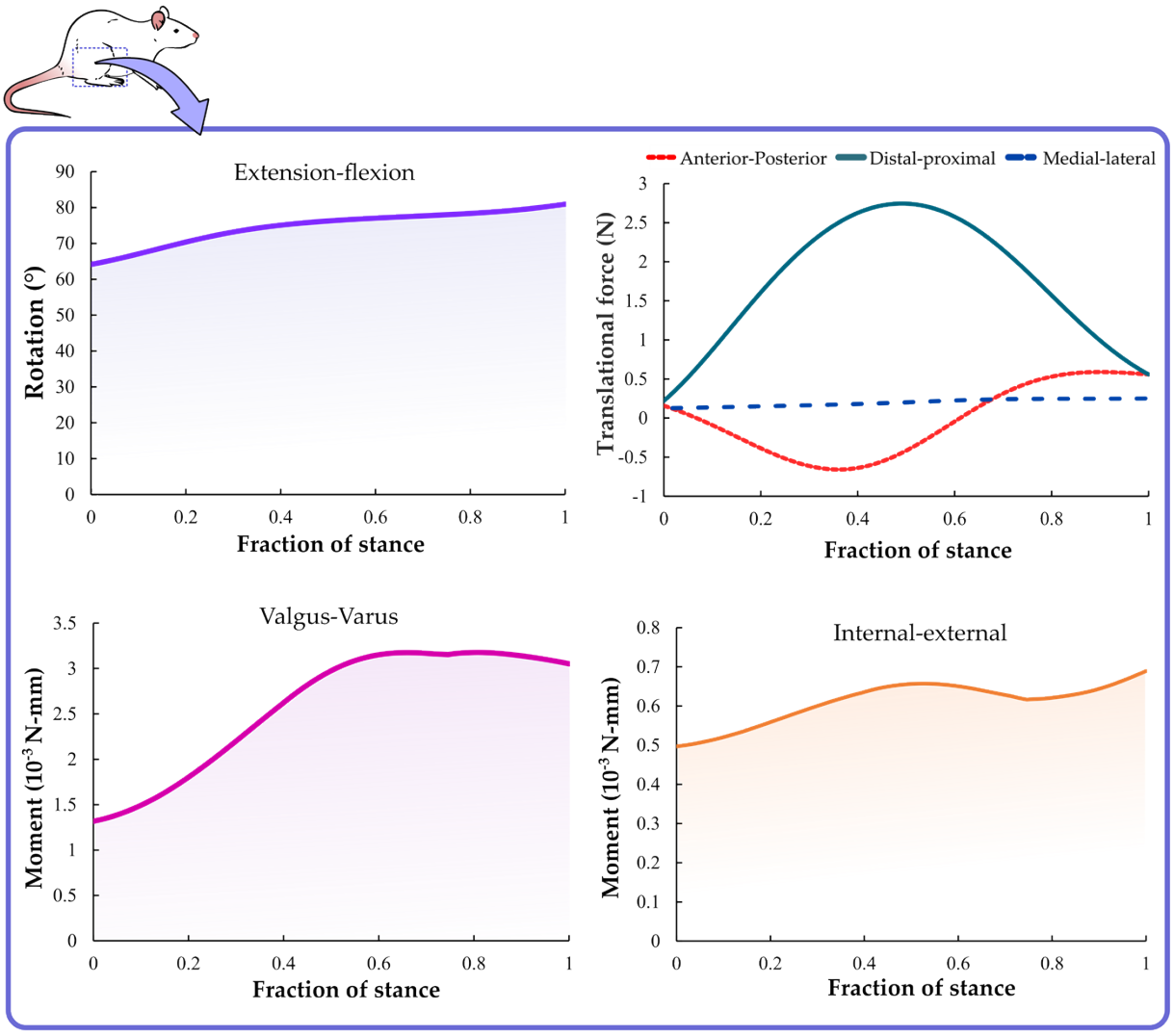

795 **Fig 3.**

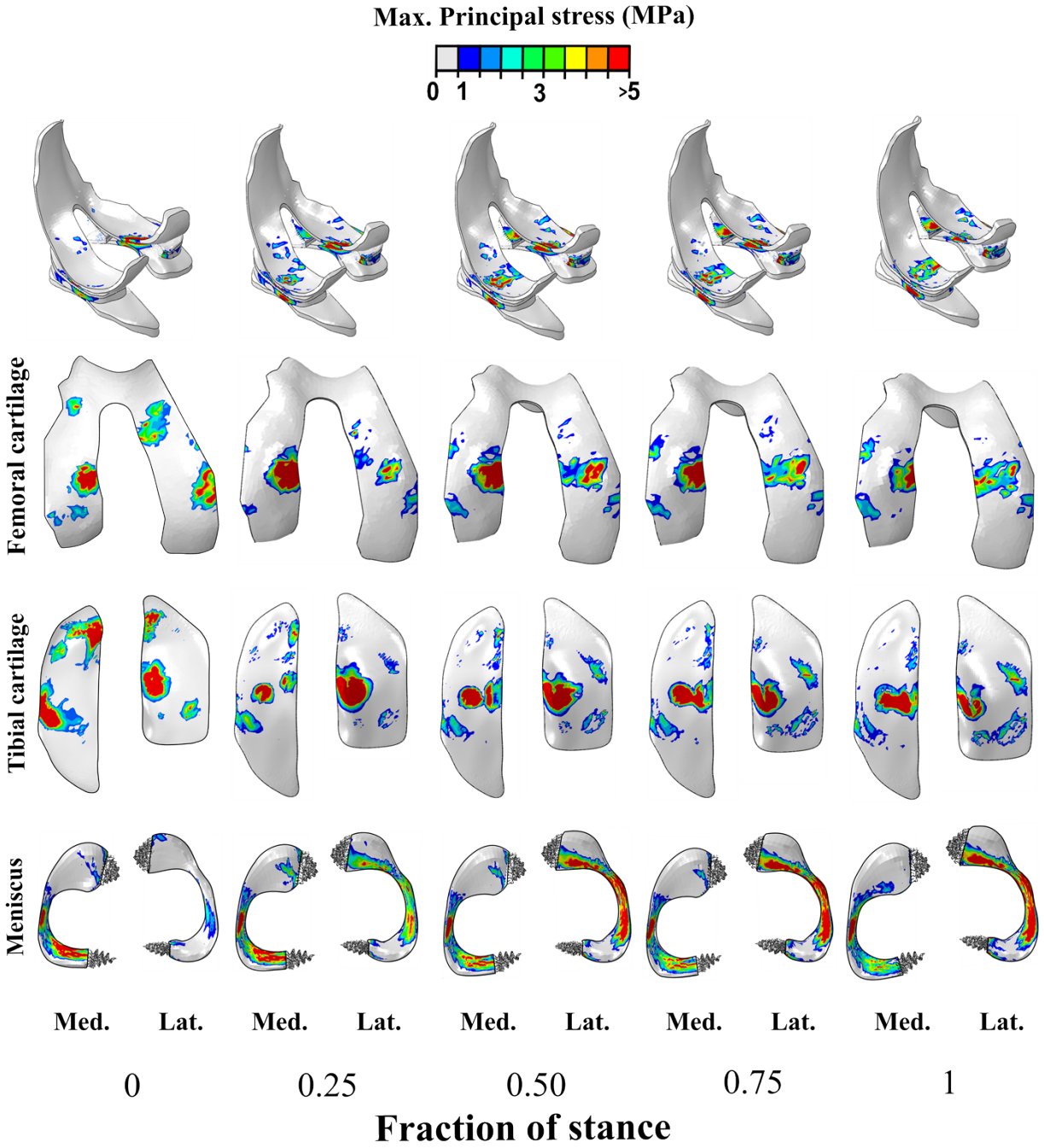

796

797

798

799

Fig 4.

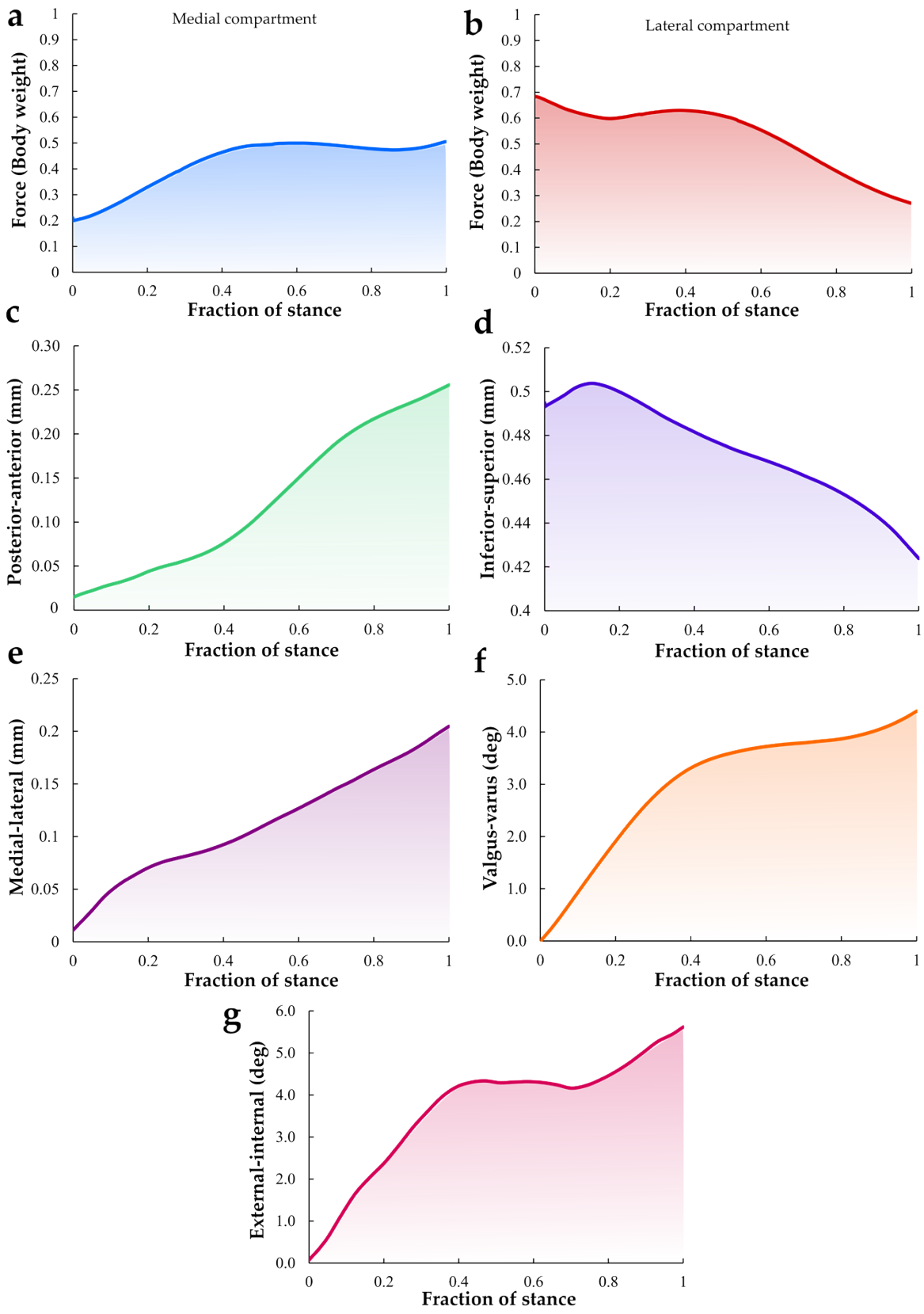

802 **Fig 5.**

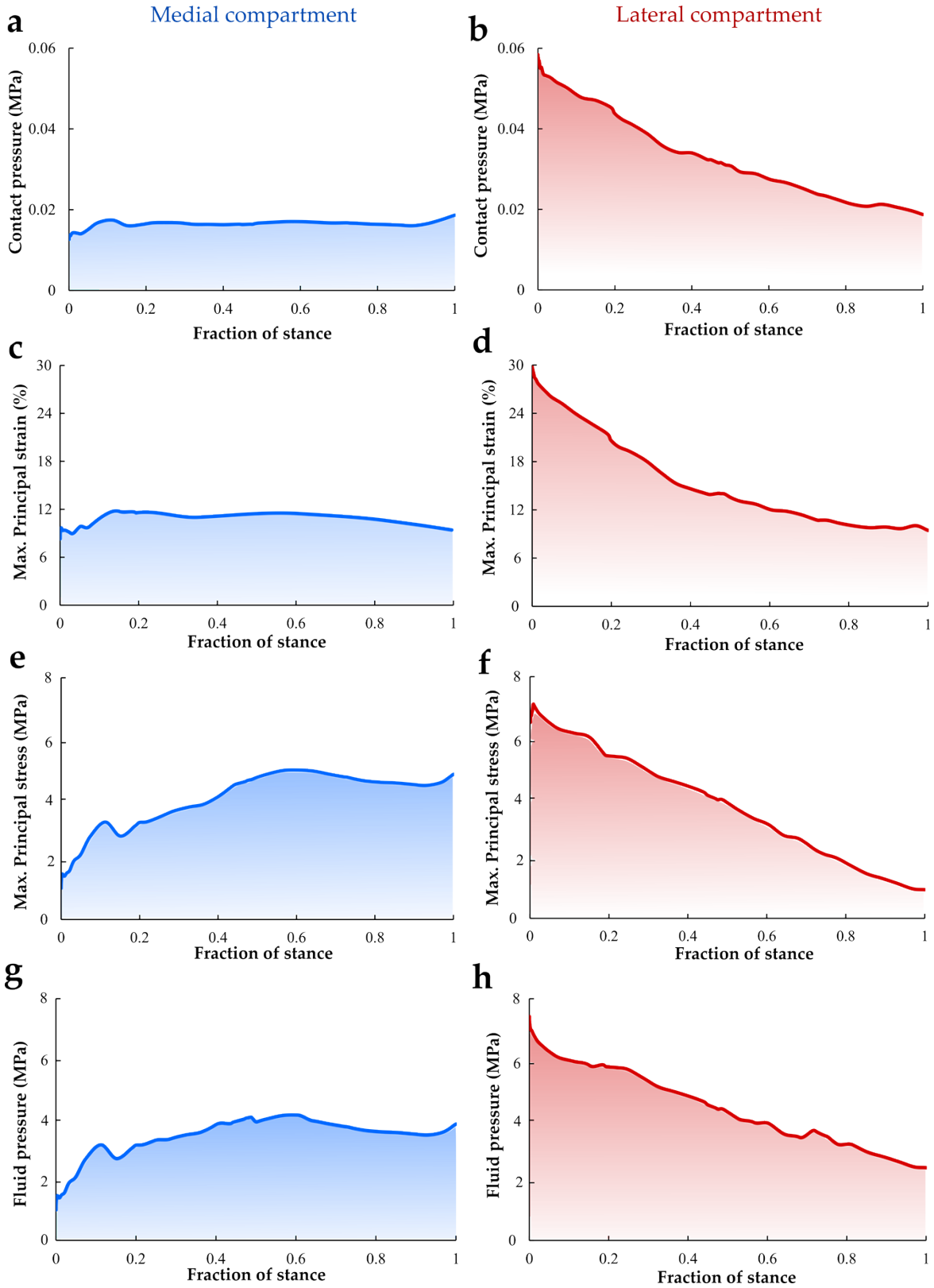

803

804 **Fig 6.**

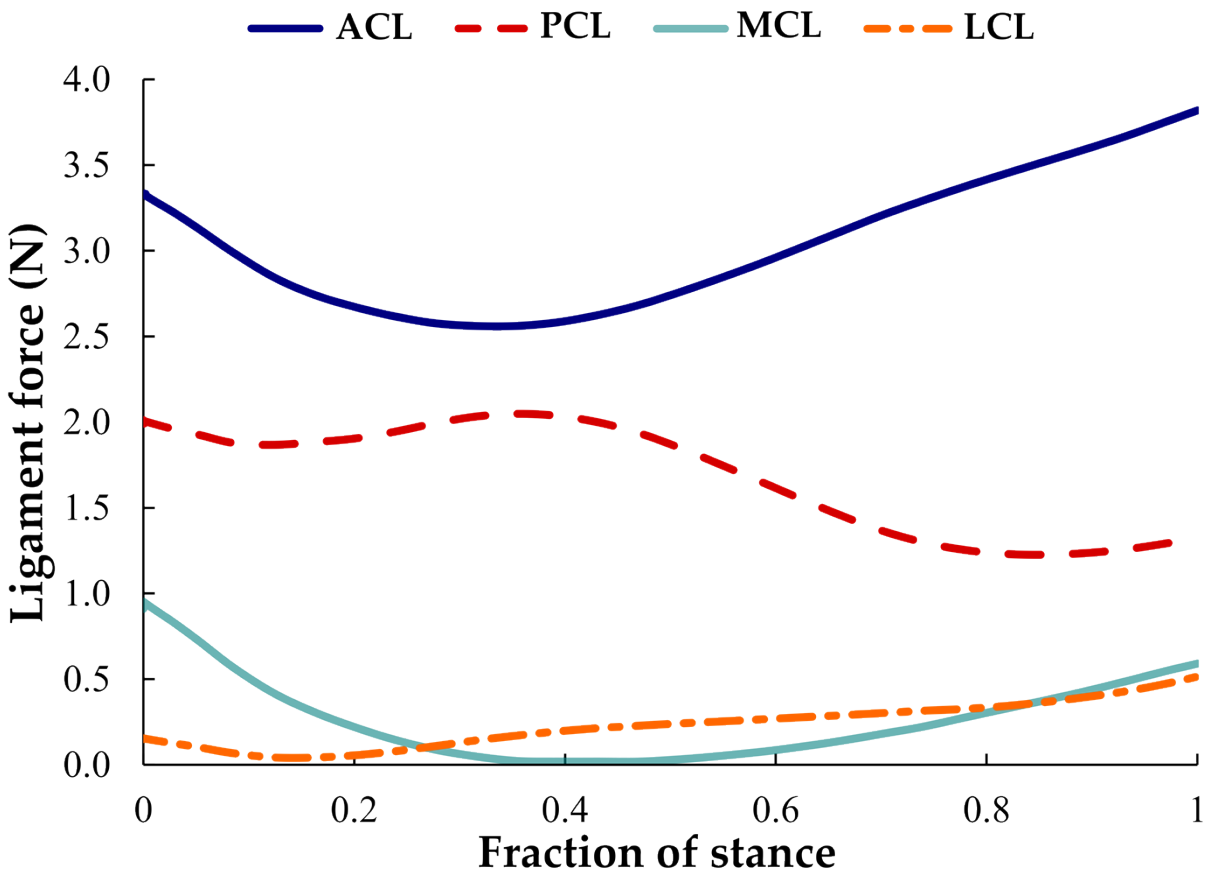

805

806

807

808

809

810

811

812

813

814

815